In situ evaluation of the transformation behaviour of NiTi-based high temperature shape memory alloys

M.A. Azeem[a], D. Dye[a,*]

[a]*Dept. Materials, Royal School of Mines, Imperial College, Prince Consort Road, South Kensington, London SW7 2BP, UK*

Abstract

Fine grained polycrystalline NiTi shape memory alloys containing 15 at.% Hf and Zr and zero or 3 at.% Cu fabricated by ingot metallurgy were investigated using *in situ* synchrotron X-ray diffraction in order to examine the viability of producing stable and affordable high temperature shape memory alloys. The alloys produced had a high thermal hysteresis, in excess of 70 °C but A_f temperatures of over 250 °C were obtained for $Ni_{50}Ti_{35}Hf_{15}$. 3 at.% Cu additions did not significantly reduce the per-cycle degradation of transformation temperatures but did reduce the transformation temperatures. The evolution of the lattice parameters during the first five thermal cycles was observed. Negative thermal expansion was found in the $b_{B19'}$ cell direction in all the alloys examined and significant deviations in the lattice parameters in the region of transformation were found. A per-cycle evolution in the end-point B19′ lattice parameters was observed, but no such evolution was found for the B2 phase, which is rationalised by appealing to the increase in population of interface dislocations.

Keywords: NiTi, shape memory alloys, X-ray diffraction, synchrotron

1. Introduction

Shape memory alloys (SMAs) operate by a martensitic, long-range diffusionless transformation from one crystal structure to another; the transformation may be ~~superelastic~~ stress induced or it may be temperature induced. In the former case, they are of utility as low modulus, high strain springs and in the latter as thermal actuators. They are also used as one-time devices to provide a deployable structure *via* the remarkable martensite memory phenomenon, for example in space craft. In the actuator application, it is desirable to possess high temperature shape memory alloys (HTSMAs) with much higher actuation temperatures that would be applicable to, for example, gas turbine compressor ducts and noise suppression systems [1–3].

Near-equiatomic NiTi has transformation temperatures in the range of ~~0 to 20 °C~~ −92 to 65 °C for the on-cooling transformation and ~~30 – 80°C~~ −47 to 107 °C for the on-heating transformation [4] . The existence of a hysteresis in the transformation temperatures must be due to the presence of non-recoverable defects, such as interface dislocations, since purely elastic and thermodynamic contributions to the driving force would result in a ideally reversible transformation. Indeed, when the interface strain is minimised according to the phenomenological theory of martensite crystallography, the hysteresis is also minimised [5–7].

There are three ~~common~~ approaches to altering the transformation temperatures; (i) varying the Ni:Ti stoichiometry within the narrow range possible for the NiTi phase [8, 9], (ii) by intentional or unintentional alloying with interstitial elements, *e.g.* C or O [8, 10], or (iii) by stoichiometric addition of ternary [11–16] or quaternary [11, 13, 14] alloying elements. Approach (i) is difficult to deploy in industrial practice, because it requires finer control of the Ni:Ti ratio in the melt than can readily be achieved. Also, drastic reduction in transformation temperatures is observed in alloys with higher Ni content [8]. Approach (ii), additions of carbon or oxygen do not have a direct effect on transformation temperature, rather both elements preferentially combine with Ti to form stable compounds leaving the matrix Ni rich and therefore resulting in reduction in transformation temperatures [8]. The restriction over compositional stoichiometry to remain in vicinity of equiatomic composition observed in binary NiTi is also extended to certain NiTi based ternary alloys [17, 18] *via* the formation of pseudo binaries [19]. Therefore, in ternary and quaternary alloys (approach iii) it is desirable to maintain the $(Ni,X_1):(Ti,X_2)$ ratio in vicinity of 1:1, where X_1 and X_2 are third and/or fourth element substitutions for Ni and Ti respectively. Most substitutions for Ni, *e.g.* with Co, Fe or Cr lead to reductions in transformation temperature, whereas substitution of Hf or Zr for Ti have been observed, at least by differential scanning calorimetry, to lead to an increase in transformation temperatures. Alternatively, Pt [12], Pd [12, 20, 21] or Au [12] substitutions for Ni are attractive, but these are unlikely to be economically viable except for niche low volume applications such as thin films or for space vehicles.

A major problem for the widespread deployment of a practical SMA actuator is functional stability; frequently it is observed that the transformation temperatures and strain evolve on repeated, thermomechanical [22–25] or even just thermal cycling under a constant load [26]. The prospect is raised of ei-

*Corresponding author
Email address: david.dye@imperial.ac.uk (D. Dye)

ther an impaired fatigue response or of the on-cooling transformation dropping below the ambient temperature of the device environment, and hence cessation of function. It is usually felt that this evolution is due to build up of defects, such as dislocations produced at the martensite-austenite interface [27]. In a Cu based SMA dislocations have even been observed to serve as heterogeneous martensite nucleation sites [28]. Further to this, Simon *et. al.* [29] observed multiplication of dislocations in NiTi single crystals during thermal cycling. These studies emphasise the importance of defects in shape memory alloys. Therefore much research in this field has focussed on mechanical processing to provide a stable defect population, *e.g.* by the production of a very fine grain size and/or by the introduction of additional stable intermetallics such as $TiNi_3$ [30], Ti_2Ni [31] and Ti_3Ni_4 [32, 33], although a clear mechanistic understanding of the role of defects and their evolution during transformation is still elusive.

The high temperature NiTi phase is found to be the B2 ordered *bcc* structure and the low temperature phase is usually found to be produced by an orthorhombic distortion and shear of the B2 phase to a monoclinic B19′ [34], but other related crystal structures are also possible. For example, Cu additions in near-equiatomic NiTi are observed to promote a two-step transformation from the B2 phase to an orthorhombic B19 and then shear to the monoclinic B19′ structure for Cu additions in excess of 9 at.% [35]. Such two-step transformation paths are supposed to lead to enhanced stability, by providing fewer habit plane variant (HPV) possibilities.

Much of the existing literature is confined to ternary additions and provides only macroscopic symptomatic extensive property data such as that provided by dilation or calorimetry. Such approaches are appealing on economic grounds but provide only limited insight into the evolution of the material as the transformation proceeds, into the nature of the interface plane or into the way in which the transformation strains are accommodated by elasticity when a two phase mixture is present. Softening of elastic constants prior to martensitic transformation is thought to be the primary factor in stability of transforming phases [36]. Therefore, the elastic modulus of parent lattice is believed to influence the transformation temperatures. However, there is limited experimental evidence to support this in current literature. In this paper we examine the transformation behaviour of $Ni_{50}Ti_{35}X_{15}$ alloys with and without the substitution of 3 at.% Cu for Ni, where X= Hf or Zr. Hf and Zr additions are attractive because both have reasonable solubility in NiTi [37], they do not possess very high density and their cost is moderate. Synchrotron X-ray powder diffraction is employed to examine the transformation behaviour, except in case of $Ni_{47}Ti_{35}Zr_{15}Cu_3$, on repeated no-load thermal cycling and the diffraction elastic constants of each phase are evaluated, providing a first estimate of the effect of alloying on the single crystal properties.

2. Experimental Description

The alloys were prepared by Vacuum Arc Melting (VAM) 3N or higher purity constituent elements (lump < 5 mm in max. dimension) in Ar. Small ∼ 50 g ingots were melted and remelted 5-6 times with inter-melt flipping followed by homogenization at 900°C for 24 h. They were then encapsulated in steel cans and hot rolled to a thickness of 3±0.5 mm at 900°C in order to produce a fine grained microstructure so as to obtain complete Debye-Scherrer rings, Figure 1a, during Synchrotron X-ray diffraction (SXRD). Intact $Ni_{50}Ti_{35}Hf_{15}$ and $Ni_{47}Ti_{35}Hf_{15}Cu_3$ rolled strip was produced but cracking was observed in the $Ni_{50}Ti_{35}Zr_{15}$ alloy.

Table 1: Average matrix compositions measured using EDX (at.%) for each alloy examined.

	$Ni_{50}Ti_{35}Hf_{15}$	$Ni_{50}Ti_{35}Zr_{15}$	$Ni_{47}Ti_{35}Hf_{15}Cu_3$	$Ni_{47}Ti_{35}Zr_{15}Cu_3$
Ni	49.7	49.5	47.0	46.2
Ti	35.0	36.8	36.4	36.3
Hf	15.3	–	14.2	–
Zr	–	13.7	–	14.8
Cu	–	–	2.5	2.7

The SXRD experiments were performed in transmission mode, Figure 1b, at the ID15B monochromatic beamline at the ESRF, France. The incident beam wavelength was 0.1427 Å and a Pixium 4700 [38] area detector mounted at a distance of 1.228 m from sample was used to record complete Debye-Scherrer patterns. Polished, flat dogbone specimens with gauge 1.5×1.5×15 mm in size were electro-discharge machined, except for $Ni_{50}Ti_{35}Zr_{15}$ where a 1.5×1.5×8 mm gauge stick specimen was used due to the unavailability of large intact uncracked sample lengths after rolling. An Instron electro thermomechanical testing (ETMT) machine was used for resistance heating and accurate temperature measurements were ensured by mounting an R type thermocouple on the top surface of the gauge volume of the X-ray beam; the beam was used for alignment. To ensure good electrical contact at grips, a small load of 5 MPa was applied during thermal cycling.

Using a 0.5×0.6 mm beam adequate diffraction images could be obtained in 0.4 s during heating and cooling at a rate of $1°Cs^{-1}$. Intensity (integrated across 360° azimuthal angle) *vs.* diffraction angle (2θ) patterns, Figure 1c, were obtained from the 2D images by using FIT2D [39]. A ceria standard was used to calibrate the diffractometer. Each pattern was Rietveld refined [40] using the Generalized Structure Analysis System (GSAS) [41, 42] to evaluate the lattice parameters and volume fractions of each phase. The strong rolling texture produced, which evolved during the experiments, meant that a model texture was refined during Rietveld fitting; χ^2 of less than 1 were obtained in the majority of cases. The atomic positions obtained for B19′ were consistent with those reported by Cuevas *et al.* [43].

Differential scanning calorimetry (DSC) was performed on a Mettler Toledo DSC 822^e instrument using aluminium as a reference. Heating and cooling was performed at a rate of $10\ °Cs^{-1}$ in a nitrogen gas environment. Large area Energy Dispersive X-ray Spectroscopy (EDX) measurements were performed in an SEM to obtain the alloy compositions actually achieved.

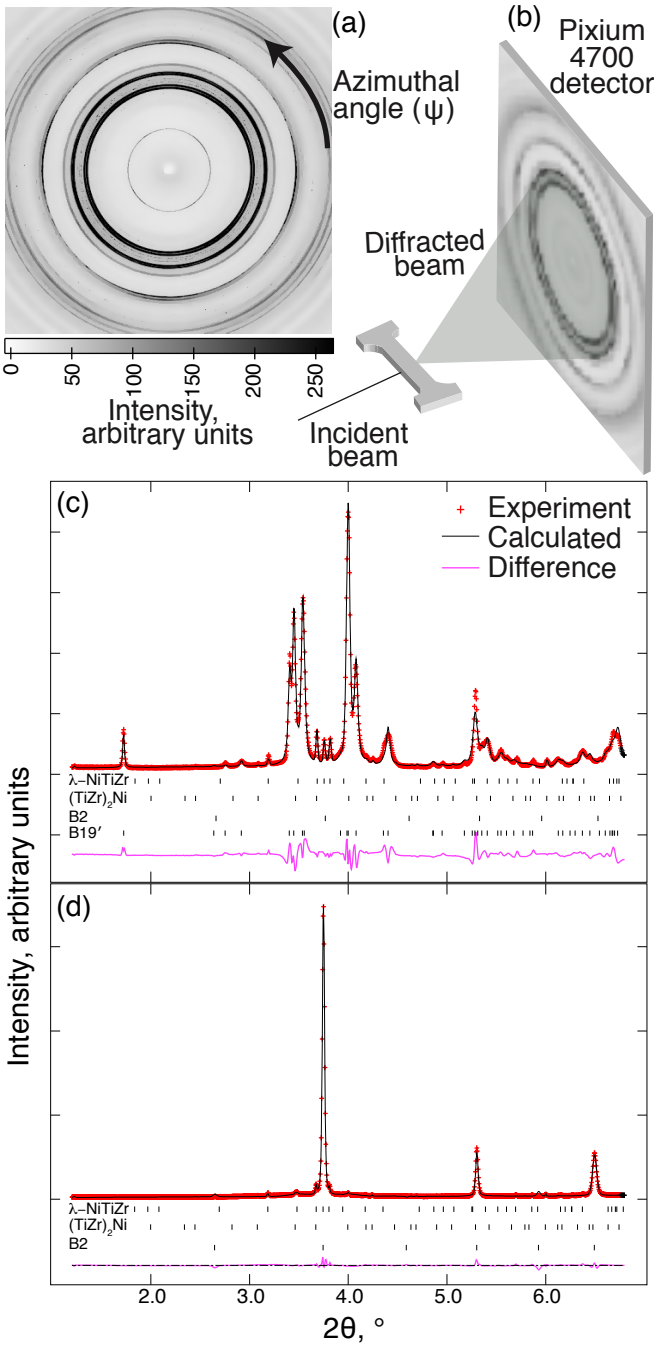

Figure 1: (a) diffraction pattern at 0% strain showing B19′rings in $Ni_{50}Ti_{35}Zr_{15}$ HTSMA, (b) Synchrotron X-ray diffraction experimental setup, (c) X-ray diffraction spectra at room temperature; integrating intensity across complete diffraction ring and (d) corresponding spectra at elevated temperature in the B2 phase.

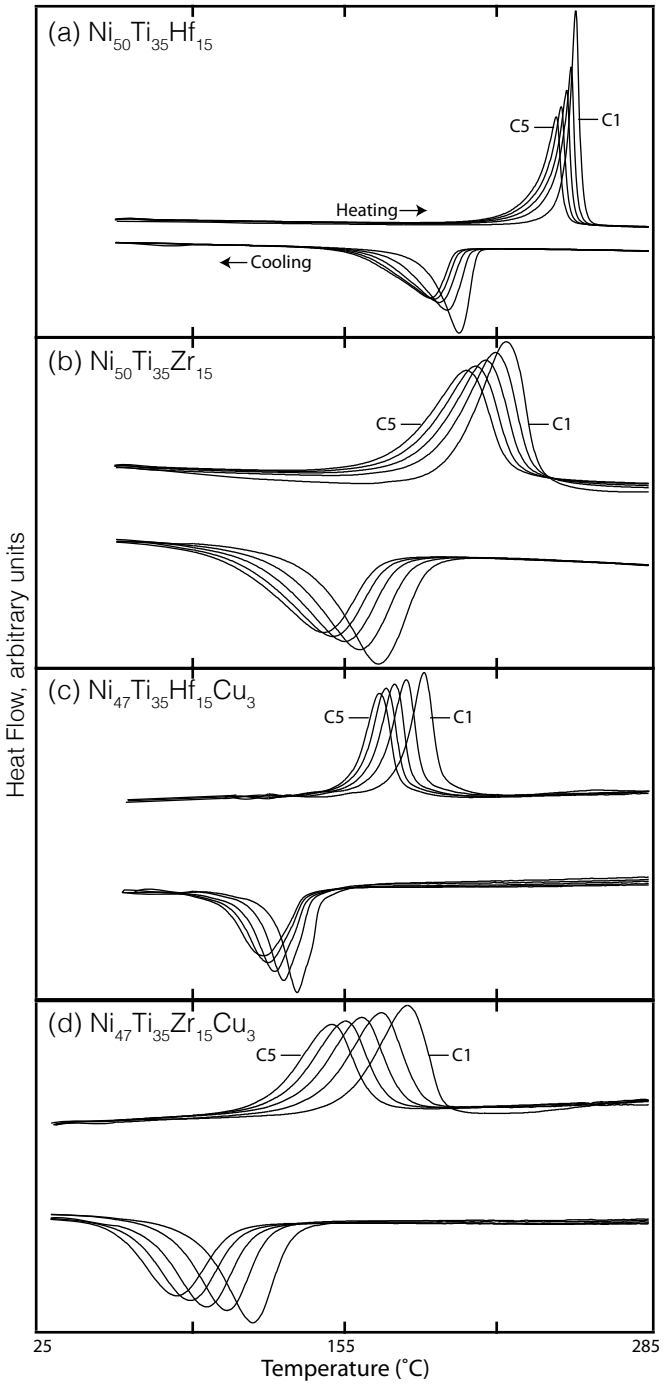

Figure 2: Differential Scanning Caloriemetry results obtained for five heating and cooling cycles in the as-rolled alloys.

3. Results and Discussion

The average matrix compositions of each alloy measured using EDX are provided in Table 1. Invariably a small amount of $(Ti,X)_2Ni$ (X=Hf or Zr) phase was observed in all alloys and an additional Laves phase, λ, was observed in $Ni_{50}Ti_{35}Zr_{15}$ [44], Figures 1c and 3. Precipitation of these additional phases during solidification and/or homogenization will have altered the matrix stoichiometry from the desired (Ti,X):(Ni,Cu) ratio of 1. This variation was of the order of ≈1.5% in $Ni_{50}Ti_{35}Zr_{15}$ and $Ni_{47}Ti_{35}Zr_{15}Cu_3$ but was much lower in alloys with the Hf addition, implying that Hf widens the NiTi phase field and/or reduces on-solidification partitioning of Ti.

The DSC response of the homogenized and rolled alloys is presented in Figure 2. The first cycle transformation temperatures for each of the alloys are provided in Table 2. $Ni_{50}Ti_{35}Hf_{15}$ showed the highest transformation temperatures,

Table 2: Transformation temperatures in the alloys examined. The top section lists the first cycle temperatures evaluated using DSC and the bottom section lists the temperatures for all five thermal cycles (C1–C5) evaluated using SXRD. 'Hf' denotes in $Ni_{50}Ti_{35}Hf_{15}$, 'Zr' $Ni_{50}Ti_{35}Zr_{15}$, 'HfCu' $Ni_{47}Ti_{35}Hf_{15}Cu_3$ and 'ZrCu' the $Ni_{47}Ti_{35}Zr_{15}Cu_3$ alloy. M_s–Martensite start, M_p–Martensite peak, M_f–Martensite finish, A_s–Austenite start, A_p–Austenite peak and A_f–Austenite finish, all in °C.

DSC	Hf	Zr	HfCu	ZrCu
M_s	212	201	146	130
M_p	204	169	134	115
M_f	188	125	124	97
A_s	249	195	178	161
A_p	254	225	190	183
A_f	257	238	197	196
$A_f - M_f$	69	113	73	99

SXRD		C1	C2	C3	C4	C5
Hf	M_s	189	186	185	179	178
	M_f	135	129	127	127	125
	A_s	201	198	184	178	165
	A_f	240	234	233	231	228
	$A_f - M_f$	105	105	106	104	103
Zr	M_s	201	197	192	188	183
	M_f	122	102	100	92	88
	A_s	201	186	186	171	165
	A_f	251	248	249	242	243
	$A_f - M_f$	129	146	149	150	155
HfCu	M_s	137	133	129	126	125
	M_f	85	81	77	76	75
	A_s	140	131	116	113	113
	A_f	189	182	177	177	174
	$A_f - M_f$	104	101	100	101	99

with an M_f in excess of 185°C. Zr additions were less effective and resulted in alloys with greater transformation hysteresis and a larger temperature range over which transformation occurred. Cu additions resulted in a quite appreciable reduction in the transformation temperatures, on the order of 70°C for the forward (heating) transformation and 60°C for the reverse transformation. Significant reductions in transformation temperatures were observed in all four alloys with thermal cycling; on the order of 3 – 6°C/cycle. The exo- and endothermic DSC peaks in the initial cycles are visibly asymmetric, suggesting that the last martensite to form is retarded compared to the first martensite. This and the broadening of the peaks seen on cycling are suggestive of an evolution of the defect structures (*e.g.* interface dislocations) in the material.

Monoclinic $P2_1/m$ cells can be expressed either in a so-called β [45] or a γ [46, 47] crystal setting; the γ setting is used here, consistent with [48]. Figure 3 is a panoramic view of the transformation sequence for the first thermal cycle of $Ni_{50}Ti_{35}Zr_{15}$. Individual diffraction patterns here are obtained by 360° angular integration of complete Debye-Scherrer rings (Figure 1a), each pattern representing the state of the alloy at a specific temperature. Initially in the cold condition the alloy is chiefly composed of B19′ with no B2 phase present. On heating, the (101) B19′ peak drifts from the (020) B19′, presumably as a result of anisotropic thermal expansion. Then, during transformation

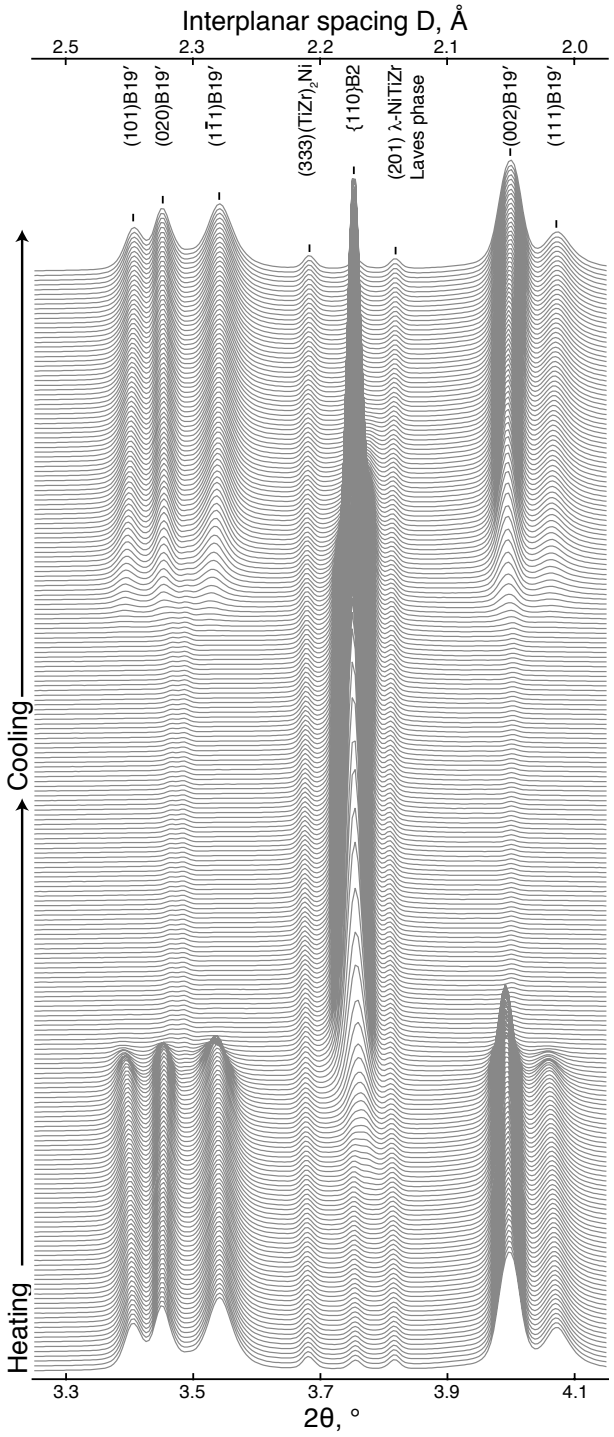

Figure 3: Evolution of the diffraction patterns during a complete heating and cooling cycle in $Ni_{50}Ti_{35}Zr_{15}$, showing the minor phases observed and the main B2↔B19′ transformation

appearance of the main {110} B2 peak is observed; followed by its redissolution on cooling and restoration of the B19′ diffraction pattern. Because of the low background and divergence achieved using this instrument, the different B19′ peaks can be clearly discerned.

In a powder diffraction pattern, the Debye - Scherrer rings

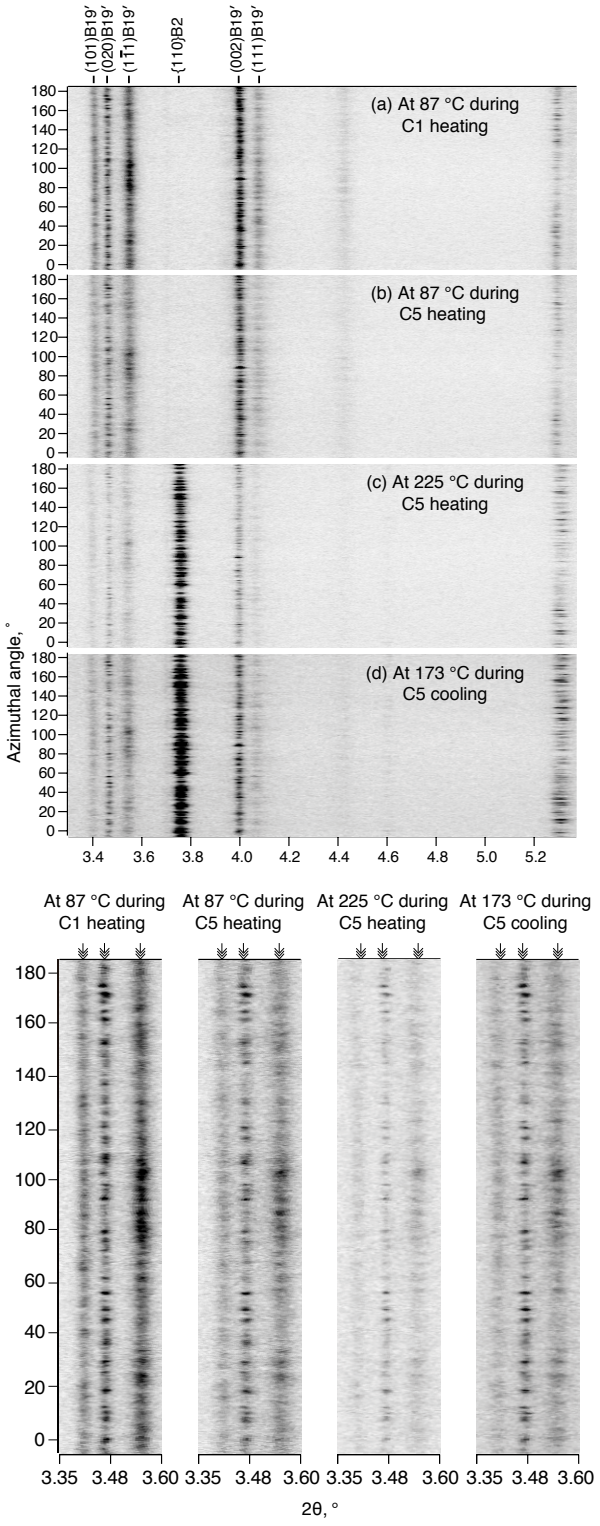

Figure 4: Diffraction patterns in $Ni_{50}Ti_{35}Hf_{15}$ at different azimuthal angles along the Debye-Scherrer rings at (a) 87 °C during heating in 1st cycle, (b) 87 °C during heating in 5th cycle (c) 225 °C during heating in 5th and (d) 173 °C during cooling in 5th cycle. The corresponding Zoomed in sections with first three peaks in (a), (b), (c) and (d) are shown at the bottom from left to right. The initial position of the peaks (during cycle 1 at 87 °C) is depicted by double arrows on top.

seize to remain circular when there are residual stresses in the sample. In the current SXRD analysis, the Debye - Scherrer rings in each alloy were analysed at various azimuthal angles by examining caked sections during thermal cycle 1 and 5. The results for $Ni_{50}Ti_{35}Hf_{15}$ are shown in Figure 4. At a constant temperature and for a given peak the 2θ peak position did not change with change in azimuthal angle indicating that the alloy was free of residual stresses.

SXRD studies were conducted on all four alloys but the diffraction information on $Ni_{47}Ti_{35}Zr_{15}Cu_3$ could not be included here due to inaccuracies in temperatures recorded during *in situ* thermal cycling on that alloy.

The evolution of the Rietveld refined phase fractions and cell parameters in the $Ni_{50}Ti_{35}Hf_{15}$ and $Ni_{50}Ti_{35}Zr_{15}$ alloys is shown in Figure 5. It is observed that the transformation proceeds more gradually in $Ni_{50}Ti_{35}Zr_{15}$ than in $Ni_{50}Ti_{35}Hf_{15}$, and that there is greater per-cycle drift, as observed in the DSC measurements. The transformation temperatures measured using the fitted diffraction data (at 10 and 90 wt.%) are also provided in Table 2. The temperatures obtained using SXRD will be less reliable than in DSC, because the heating arrangements are less isothermal using resistance heating than in a DSC, but most probably the transformation onset and completion can be measured more reliably; therefore a larger hysteresis is measured using diffraction but the absolute temperatures show slightly greater scatter. The fifth cycle austenite transformation interval ($A_f - A_s$) is 63 °C in $Ni_{50}Ti_{35}Hf_{15}$ and 78°C in $Ni_{50}Ti_{35}Zr_{15}$, while the hysteresis ($A_f - M_f$, Table 2) is also greater in $Ni_{50}Ti_{35}Zr_{15}$ than in $Ni_{50}Ti_{35}Hf_{15}$. Previously, this has been correlated to the interface plane strain [6, 20, 21].

The $Ni_{47}Ti_{35}Hf_{15}Cu_3$ alloy, in contrast, shows almost the same interval and hysteresis as the Cu-free Hf alloy, but with lower transformation temperatures. The DSC results also show a lack of improvement in hysteresis with Cu additions. The drift on cycling was also similar in the two alloys. These results suggest that, at least at this level of doping, Cu additions do not improve the functional stability of the alloy.

The Rietveld refined room temperature lattice parameters of B19′, the B2 lattice parameter at 280 °C and the corresponding unit cell volumes are listed in Table 3. Compared to binary near equiatomic NiTi [26, 45], $a_{B19'}$, $b_{B19'}$ and γ are larger, but $c_{B19'}$ is smaller . Of the three alloys, $Ni_{50}Ti_{35}Zr_{15}$ has the largest B19′

Table 3: Rietveld refined unit cell parameters (in Å except for γ in degrees) and cell volumes (in Å^3), at room temperature for B19′ and at 280°C for B2 in ~~$Ni_{35}Ti_{50}Hf_{15}$~~ $Ni_{50}Ti_{35}Hf_{15}$, $Ni_{50}Ti_{35}Zr_{15}$ and $Ni_{47}Ti_{35}Hf_{15}Cu_3$. The lattice parameters of near equiatomic NiTi from Otsuka *et al.* [45] are also tabulated in the γ monoclinic angle setting. The uncertainties are provided in parentheses.

	NiTi	~~$Ni_{35}Ti_{50}Hf_{15}$~~	$Ni_{50}Ti_{35}Hf_{15}$	$Ni_{50}Ti_{35}Zr_{15}$	$Ni_{47}Ti_{35}Hf_{15}Cu_3$
$a_{B19'}$	2.889	3.0321(3)	3.0382(4)	3.0369(4)
$b_{B19'}$	4.622	4.8408(5)	4.8548(5)	4.8191(7)
$c_{B19'}$	4.120	4.0826(4)	4.0872(3)	4.0988(3)
$\gamma_{B19'}$	96.8	102.40(1)	102.51(1)	101.46(2)
a_{B2}	–	3.08079(4)	3.08430(8)	3.08780(6)
$V_{B19'}$	–	58.524(8)	58.853(8)	58.79(1)
V_{B2}	–	29.241(1)	29.341(2)	29.441(2)

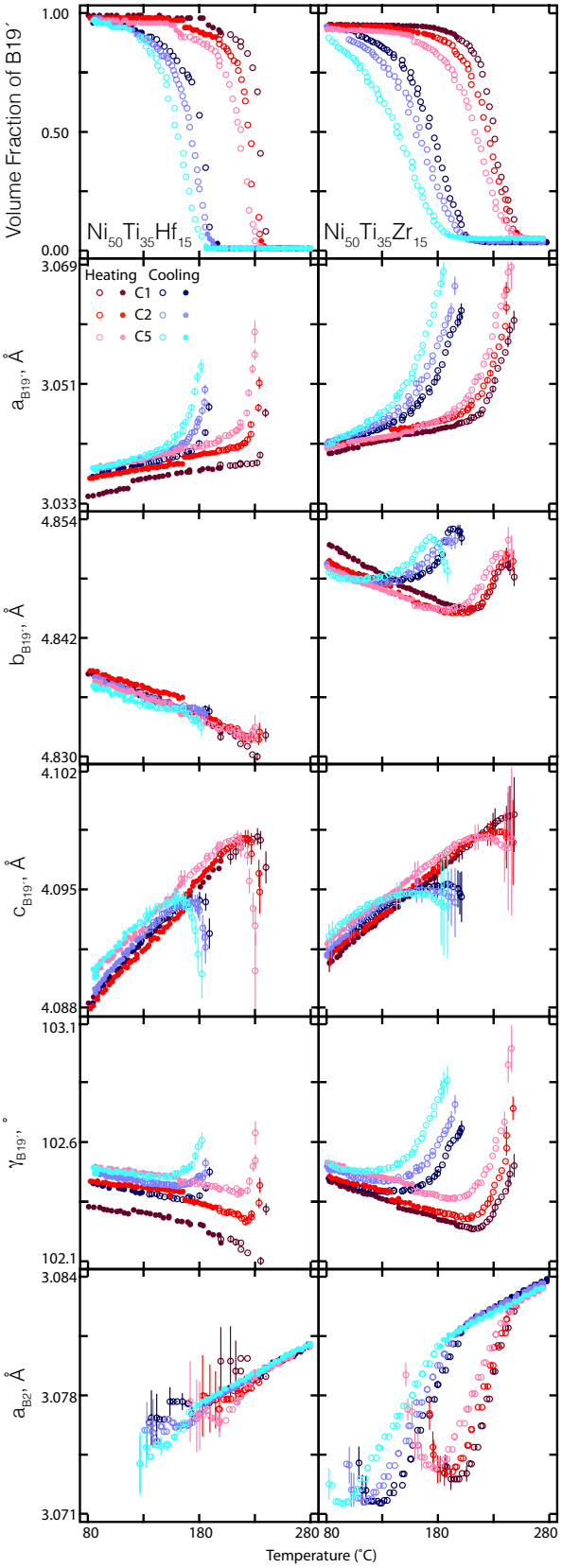

Figure 5: Lattice evolution in $Ni_{50}Ti_{35}Hf_{15}$ and $Ni_{50}Ti_{35}Zr_{15}$. Solid symbols are in single phase region and open symbols during transformation.

unit cell and $Ni_{47}Ti_{35}Hf_{15}Cu_3$ has the largest B2 unit cell. The lattice parameters of both phases in $Ni_{50}Ti_{35}Zr_{15}$ are larger than that in $Ni_{50}Ti_{35}Hf_{15}$, in spite of the fact that the atomic radii of both Hf and Zr are nearly the same [49, 50]. Surprisingly, the stoichiometric substitution of 3 at.% Cu for Ni on the Ni sublattice, which has a similar atomic radius to Ni [49], increases the B19′ and B2 unit cell volumes, by 0.45% and 0.68% respectively. The per cycle evolution of B19′ lattice parameters at 85 °C and the B2 lattice parameter at 265 °C in all three alloys is provided in Appendix A.

The linear change in lattice parameter on heating and cooling away from the transformation regime is obviously interpreted as being due to thermal expansion. The negative change in $b_{B19'}$ with temperature can therefore be attributed to a negative thermal expansion in that direction. A negative thermal expansion coefficient in $b_{B19'}$ has also been observed in near equiatomic NiTi in data collected as part of the study reported in [26]. This is also evident from the negative changes with temperature in the $(11\bar{1})$, $(10\bar{1})$ and $(20\bar{1})$ interplanar distances reported by Qiu *et al.* [51], indicating a negative thermal expansion coefficient along $c_{B19'}$ (or $b_{B19'}$ in a γ monoclinic angle setting). The thermal expansion coefficients of all three B19′ crystallographic axes and of B2 in the three HTSMAs investigated are listed in Table 4.

Large dilations and constrictions in the Rietveld-refined lattice parameters are observed in both the -Hf and -Zr alloys during transformation, Figure 5. For example, the $c_{B19'}$ of $Ni_{50}Ti_{35}Hf_{15}$ in 5th thermal cycle undergoes $\approx 0.2\%$ compression (less the thermal expansion) in the 5th thermal cycle between 200 and 230°C. The $a_{B19'}$ undergoes a 0.016 Å dilation in the same temperature regime and the monoclinic angle increases by in excess of 0.3° but no such abrupt changes appear obvious in case of $b_{B19'}$. On the contrary, large variations in $b_{B19'}$ in $Ni_{50}Ti_{35}Zr_{15}$ are observed during final stages of transformation. During heating, initially the B2 lattice in both alloys undergoes a contraction followed by a narrow temperature regime where it remains unchanged and then eventually undergoes a steep dilation during the final stages of transformation. The gradient da_{B2}/dT in final stages of transformation reduces with each thermal cycle (particularly in -Zr) and the sequence of events are exactly reversed during cooling in each cycle. The magnitude of change in the $Ni_{50}Ti_{35}Zr_{15}$ B2 lattice is much larger than that in $Ni_{50}Ti_{35}Hf_{15}$. The role of transformation stresses due to the texture-related production / dissolution

Table 4: Coefficient of thermal expansion in the three crystallographic axes of B19′ and B2 in ~~$Ni_{35}Ti_{50}Hf_{15}$~~, $Ni_{50}Ti_{35}Zr_{15}$ and $Ni_{47}Ti_{35}Hf_{15}Cu_3$, expressed in $\times 10^{-6}°C^{-1}$

	~~$Ni_{35}Ti_{50}Hf_{15}$~~	$Ni_{50}Ti_{35}Hf_{15}$	$Ni_{50}Ti_{35}Zr_{15}$	$Ni_{47}Ti_{35}Hf_{15}Cu_3$
$a_{B19'}$	10	13	20	
$b_{B19'}$	-8	-13	-5	
$c_{B19'}$	18	13	14	
$\gamma_{B19'}$	-5	-16	-7	
a_{B2}	9	11	11	
$V_{B19'}$	0.17	0.17	0.17	
V_{B2}	0.34	0.34	0.34	

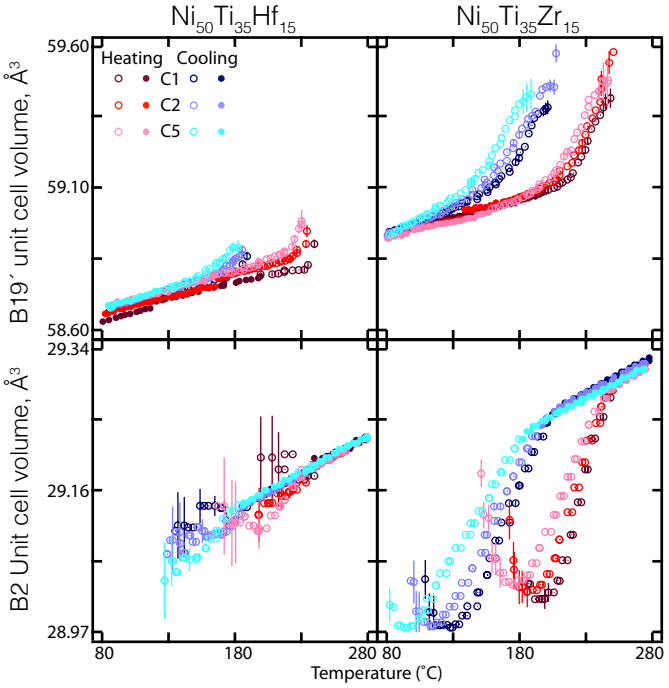

Figure 6: B2 and B19′ unit cell volume evolution in $Ni_{50}Ti_{35}Hf_{15}$ and $Ni_{50}Ti_{35}Zr_{15}$. Solid symbols are in single phase region and open symbols during transformation.

of habit plane variants of the martensite has been examined by selective examination of the diffraction patterns from different ring segments, and the dilations were unchanged. This suggests that residual stresses were not the primary cause of this behaviour. The appearance of these shifts in lattice parameter during transformation is, as far as we are aware, a new observation and this is examined in more detail elsewhere [52].

At the end of each thermal cycle, the B19′ lattice parameters undergo a permanent shift or step. For example, the initial room temperature $b_{B19'}$ lattice parameter in $Ni_{50}Ti_{35}Zr_{15}$ was 4.8548 Å and after first thermal cycle the new $b_{B19'}$ room temperature lattice parameter was 4.8515 Å, a decrease of 0.003 Å. This shift reduces in subsequent cycles. However, the B2 lattice in both alloys does not show such per-cycle evolution and away from transformation regime the a_{B2} at a given temperature in each cycle are the same.

This finding can be rationalised by appealing to the evolution of the defect state in the materials; for instance an evolution in B2 peak width with cycling was observed which, at least in NiTi, appears to be due to the production of dislocations [26, 29]. In the B19′, these dislocations therefore result in an evolution in the lattice parameters due to the relaxation of the interface stresses by dislocations.

The evolution of unit cell volumes of B2 and B19′ in both alloys with temperature are provided in Figure 6. Away from transformation, the B19′ unit cell volume in $Ni_{50}Ti_{35}Hf_{15}$ and $Ni_{50}Ti_{35}Zr_{15}$ increases at a rate of 1×10^{-3} and 0.9×10^{-3} Å^3°C^{-1} respectively. During the transformation, the change in unit cell volume for one phase appears to be complemented by a similar change in the the other.

Table 5: Diffraction elastic constants in GPa along (020) and (002) of B19′ and {110} of B2 in ~~$Ni_{35}Ti_{50}Hf_{15}$~~ $Ni_{50}Ti_{35}Hf_{15}$ and $Ni_{47}Ti_{35}Hf_{15}Cu_3$. DECs for $Ni_{49.8}Ti_{50.2}$ from [26] are provided for comparison

	$Ni_{49.8}Ti_{50.2}$	~~$Ni_{35}Ti_{50}Hf_{15}$~~ $Ni_{50}Ti_{35}Hf_{15}$	$Ni_{47}Ti_{35}Hf_{15}Cu_3$
$E_{B19'(010)}$	156	104±3	108±6
$E_{B19'(001)}$	203	82±2	91±3
$E_{B2(110)}$	–	76±1	79±2

The evolution of the B2 and B19′ lattice parameters in $Ni_{47}Ti_{35}Hf_{15}Cu_3$ are shown in Figure 7. As in the other two alloys, the coefficients of thermal expansion here are positive for $a_{B19'}$ and $c_{B19'}$ and negative along $b_{B19'}$.

During transformation, the magnitude of dilation or contraction observed along each crystallographic axis are much smaller than the dilations in the other two alloys. For example, the maximum $a_{B19'}$ dilation in $Ni_{47}Ti_{35}Hf_{15}Cu_3$ during transformation is about 0.006, ≈ 0.7× than that observed in ~~$Ni_{35}Ti_{50}Hf_{15}$~~ $Ni_{50}Ti_{35}Hf_{15}$. Unlike in the other two alloys, the $c_{B19'}$ and the B19′ unit cell volume in $Ni_{47}Ti_{35}Hf_{15}Cu_3$ does not show large deviations from linearity. However, the changes in a_{B2} are far from linear within transformation regime. The B2 unit cell volume in this alloy increases at a rate of 0.001 Å^3°C^{-1}, similar to that in $Ni_{50}Ti_{35}Hf_{15}$, and the B19′ lattice undergoes a stepped transformation like in other two alloys. The maximum M_s temperature reported by Meng *et al.* [53] in their investigation on $Ni_{44}Ti_{36}Hf_{15}Cu_5$ ribbon samples was 150 °C which is comparable to the M_s for $Ni_{47}Ti_{35}Hf_{15}Cu_3$ observed in the current investigation.

Figure 8 shows the macroscopic dilations in all three alloys during thermal cycling along the tensile axis recorded using the ETMT cross head displacement. Since resistance heating produces a parabolic temperature profile across the sample, these changes cannot be directly related to the macroscopic strains experienced in the diffraction gauge volume at a specific temperature, but they do provide a qualitative indication of the macroscopic dilation hysteresis.

The linear displacement away from the transformation regime corresponds to the thermal dilation (on heating) or contraction (on cooling) of the B19′ and B2 phases, with the change during transformation being due to both the volume change transformation modified by the individual variant relationships, because the samples were textured. The displacements in $Ni_{50}Ti_{35}Zr_{15}$ are an order of magnitude smaller than those observed in other two alloys due to the fact that a much smaller gauge length specimen was used in that experiment.

The residual displacements at the end of each thermal cycle observed macroscopically in Figure 8 are presumably a reflection of the evolution in the B19′ lattice parameters between thermal cycles observed in Figures 4-6. Clearly, the thermal hysteresis is smallest in $Ni_{47}Ti_{35}Hf_{15}Cu_3$. This suggest that Cu additions are desirable for actuator applications. However, a corollary is necessarily that a lack of displacement hysteresis in dilatometry does not necessarily indicate stability of the transformation temperatures on thermal cycling, so the size of the displacements measured using dilatometry cannot on its own be used to rationalise the temperature stability of SMAs.

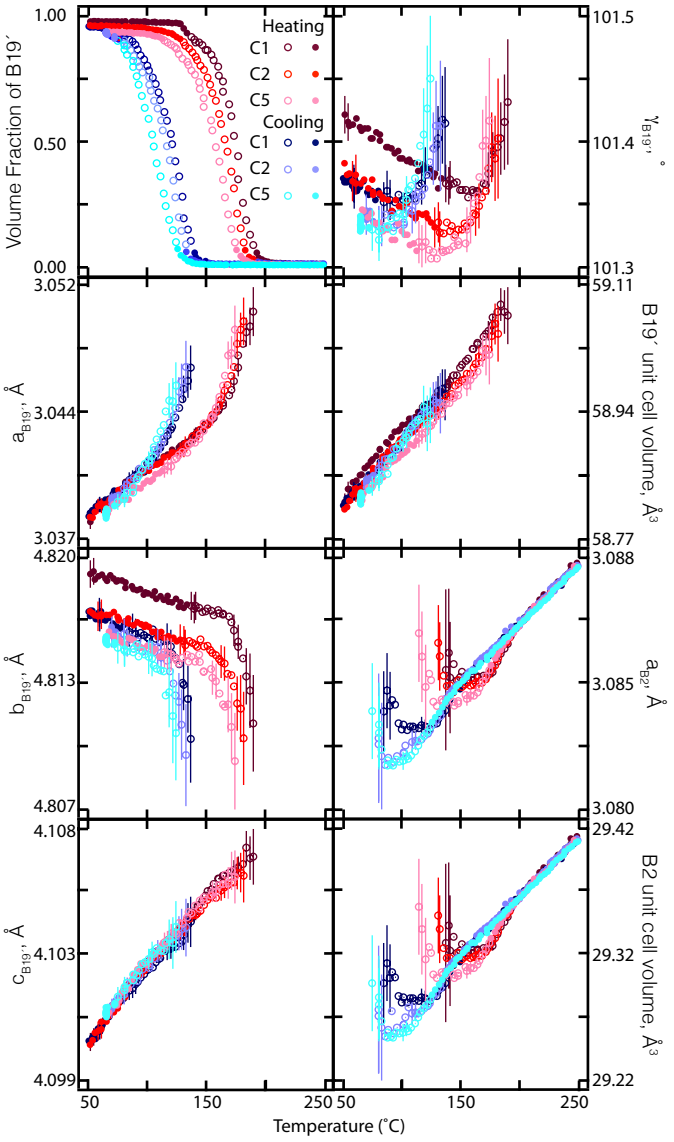

Figure 7: Lattice evolution in $Ni_{47}Ti_{35}Hf_{15}Cu_3$. Solid symbols are in the single phase region and open symbols during transformation.

At the end of the tests after five thermal cycles, each of the alloys were elastically loaded *in situ* in the B2 and B19′ states to obtain the diffraction elastic constants (DECs) of the (020) and (002) B19′ and the {110} B2 for $Ni_{50}Ti_{35}Hf_{15}$ and $Ni_{47}Ti_{35}Hf_{15}Cu_3$. Ring segments in the longitudinal direction between 80 and 100° were used to measure the changes in lattice parameter along the straining direction. The diffraction elastic constant is the relative change in lattice parameter per unit stress; it is a grain environment-modified measure of the single crystal elastic constants C_{ij}, but extraction of these requires additional modelling effort and involves a number of micromechanical assumptions [54]. The measured DECs are provided in Table 5, along with the stiffness of identical directions in equiatomic NiTi taken from [26] for comparison. The brittle $Ni_{50}Ti_{35}Zr_{15}$ alloy failed early on during loading in the B19′ state and therefore DECs for that particular alloy could not be measured.

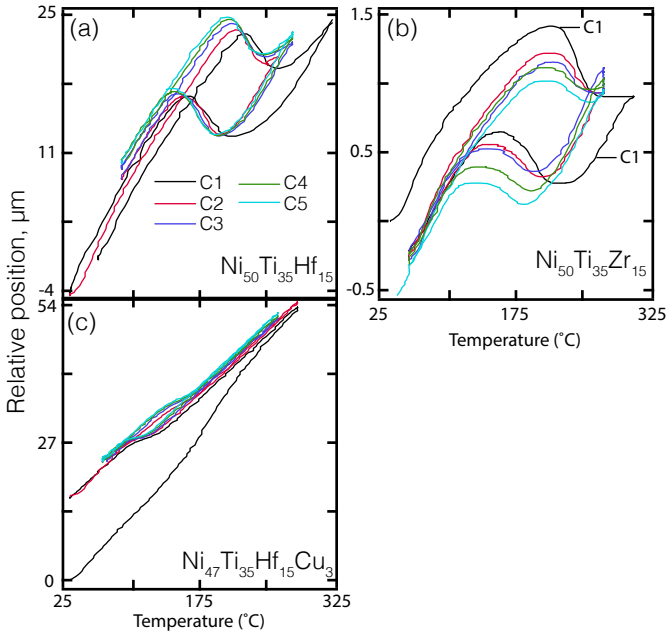

Figure 8: Dilation in macroscopic specimens during thermal cycling in (a) $Ni_{50}Ti_{35}Hf_{15}$, (b) $Ni_{50}Ti_{35}Zr_{15}$ and (c) $Ni_{47}Ti_{35}Hf_{15}Cu_3$. A magnified version of transformation regime in (c) is provided in the bottom right section.

Clearly, the B19′ in HTSMAs is less stiff than in equiatomic NiTi. Alloying also seems to affect the elastic anisotropy; in NiTi while the $E_{B19'(010)}$ is smaller than the $E_{B19'(001)}$, the reverse is observed in the HTSMAs. The ~~$Ni_{35}Ti_{50}Hf_{15}$~~ $Ni_{50}Ti_{35}Hf_{15}$ lattice appears to be slightly more compliant than $Ni_{47}Ti_{35}Hf_{15}Cu_3$.

4. Conclusions

The behaviour of hot rolled polycrystalline NiTi alloys containing 15 at.% Hf and Zr have been examined using synchrotron X-ray diffraction and the effect of a 3 at.% Cu addition studied. The following conclusions can be drawn from this work.

1. Relatively low cost Hf and Zr-containing NiTi HTSMAs can be produced with transformation temperatures significantly higher than those of conventional NiTi SMAs. However, the thermal hysteresis $A_f - M_f$ of the alloys examined here is quite large, in excess of 70°C and the functional degradation per cycle is also relatively high and therefore these alloys are not yet practical actuator materials.
2. 3 at.% Cu additions did not significantly reduce the cyclic degradation of the transformation temperatures but did result in significant reductions (> 50°C) in the transformation temperatures. However, the macroscopic dilations observed in the Cu-containing alloy were relatively small.
3. Invariably, a small fraction of $(Ti,X)_2Ni$ was observed in the alloys fabricated, but fewer of these were found in the -Hf containing alloys than the -Zr alloys. The -Zr alloy was found to be brittle.

4. A per-cycle evolution in the B19′ lattice parameters and unite cell volume was observed, but no such evolution was observed for the B2 phase. It is suggested that this may be due to the accumulation of interface dislocations.
5. For the first time peri-transformation lattice evolution in participating phases has been captured in great detail. Large dilations and constrictions in both martensite and austenite lattices are observed in all alloys, particularly in final stages of transformation. The additions of 3 at.% Cu at the expense of Ni in ~~$Ni_{35}Ti_{50}Hf_{15}$~~ $Ni_{50}Ti_{35}Hf_{15}$ seems to have a large impact on the evolution of lattices, although it does not appear to significantly alter the lattice stiffness.
6. ~~The diffraction elastic constants $E_{B19'(010)}$ and $E_{B19'(001)}$ in all alloys in the current investigation were relatively much smaller than those observed in equiatomic NiTi.~~

Acknowledgements

This work was generously funded by Rolls-Royce plc., Imperial College and the UK-India Education and Research Initiative. Assistance from Nicholas G Jones, Khandaker Rahman and Thomas Buslaps during the experiments at the ESRF is greatly appreciated. The help and advice of Nicholas G Jones with the data analysis is also greatly appreciated. The authors are thankful to Ester Buchaca Domingo and Jennifer Nekuda for their assistance with DSC.

References

[1] N. T. Birch and J. R. Webster, "Gas turbine engine exhaust nozzle having a noise attenuation device driven by shape memory material actuators," *Techreport*, p. F02F 3/02, Feb. 2006.

[2] F. T. Calkins, J. H. Mabe, and G. W. Butler, "Boeing's variable geometry chevron: morphing aerospace structures for jet noise reduction," in *Proc. SPIE*, p. 61710O, SPIE, 2006.

[3] D. J. Hartl and D. C. Lagoudas, "Aerospace applications of shape memory alloys," *Proceedings Of The Institution Of Mechanical Engineers Part G-Journal Of Aerospace Engineering*, vol. 221, no. G4, pp. 535–552, 2007.

[4] J. Frenzel, E. George, A. Dlouhy, C. Somsen, M.-X. Wagner, and G. Eggeler, "Influence of Ni on martensitic phase transformations in NiTi shape memory alloys," *Acta Materialia*, vol. 58, no. 9, pp. 3444 – 3458, 2010.

[5] J. Ball and R. James, "Proposed experimental tests of a theory of fine microstructure and the 2-well problem," *Philosophical Transactions of the Royal Society of London A*, vol. 338, no. 1650, pp. 389 – 450, 1992.

[6] J. Cui, Y. S. Chu, O. O. Famodu, Y. Furuya, J. Hattrick-Simpers, R. D. James, A. Ludwig, S. Thienhaus, M. Wuttig, Z. Y. Zhang, and I. Takeuchi, "Combinatorial search of thermoelastic shape-memory alloys with extremely small hysteresis width," *Nature Materials*, vol. 5, no. 4, pp. 286–290, 2006.

[7] Y.T. Song, X. Chen, V. Dabade, T.W. Shield, and R.D. James, "Enhanced reversibility and unusual microstructure of a phase transforming material," *Nature*, vol. 502, no. 7469, pp. 85 – 88, 2013.

[8] H. Funakubo, *Shape Memory alloys*, vol. 1. Gordon and Breach Science Publishers, New York, 1987.

[9] W. Tang, "Thermodynamic study of the low-temperature phase B19? and the martensitic transformation in near-equiatomic Ti-Ni shape memory alloys," *Metallurgical and Materials Transactions A*, vol. 28, pp. 537–544, Mar. 1997.

[10] J. Frenzel, Z. Zhang, C. Somsen, K. Neuking, and G. Eggeler, "Influence of carbon on martensitic phase transformations in NiTi shape memory alloys," *Acta Materialia*, vol. 55, pp. 1331–1341, Feb. 2007.

[11] D. N. AbuJudom, P. E. Thoma, M.-Y. Kao, and D. R. Angst, "High transformation temperature shape memory alloys," *US patent*, May 1992.

[12] P. M. Huisman-Kleinherenbrnik, *On the martensitic transformation temperatures in NiTi and their dependence on alloying elements*. PhD thesis, University of Twente, University of Twente, 1991.

[13] J. H. Mulder, *Investigation of high temperature shape memory alloys from the Ni-Ti-Zr and Ni-Ti-Hf systems*. PhD thesis, University of Twente, Twente University, 1995.

[14] J. Van Humbeeck, "High Temperature Shape Memory Alloys," *Journal of Engineering Materials and Technology*, vol. 121, no. 1, pp. 98–101, 1999.

[15] G. S. Firstov, J. Van Humbeeck, and Y. N. Koval, "Comparison of high temperature shape memory behaviour for ZrCu-based, Ti–Ni–Zr and Ti–Ni–Hf alloys," *Scripta Materialia*, vol. 50, pp. 243–248, Jan. 2004.

[16] M. Zarinejad, Y. Liu, and T. J. White, "The crystal chemistry of martensite in NiTiHf shape memory alloys," *Intermetallics*, vol. 16, pp. 876–883, July 2008.

[17] Y. Xu, S. Shimizu, Y. Suzuki, K. Otsuka, T. Ueki, and K. Mitose, "Recovery and recrystallization processes in Ti?Pd?Ni high-temperature shape memory alloys," *Acta Materialia*, vol. 45, pp. 1503–1511, Apr. 1997.

[18] R. D. Noebe, S. L. Draper, M. V. Nathal, and E. A. Crombie, "Precipitation hardenable high temperature shape memory alloys," *Techreport*, Mar. 2006.

[19] R. Noebe, "Proceedings of SPIE," in *Smart Structures and Materials 2005: Active Materials: Behavior and Mechanics*, pp. 364–375, SPIE, May 2005.

[20] R. Delville, D. Schryvers, Z. Zhang, and R. D. James, "Transmission electron microscopy investigation of microstructures in low-hysteresis alloys with special lattice parameters," *Scripta Materialia*, vol. 60, no. 5, pp. 293–296, 2009.

[21] R. Delville, S. Kasinathan, Z. Zhang, J. Van Humbeeck, R. D. James, and D. Schryvers, "Transmission electron microscopy study of phase compatibility in low hysteresis shape memory alloys," *Philosophical Magazine*, vol. 90, no. 1-4, pp. 177–195, 2010.

[22] G. Eggeler, E. Hornbogen, A. Yawny, A. Heckmann, and M. Wagner, "Structural and functional fatigue of NiTi shape memory alloys," *Materials Science and Engineering A*, vol. 378, pp. 24–33, July 2004.

[23] J. Ma, I. Karaman, H. J. Maier, and Y. I. Chumlyakov, "Superelastic cycling and room temperature recovery of $Ti_{74}Nb_{26}$ shape memory alloy," *Acta Materialia*, vol. 58, no. 6, pp. 2216–2224, 2010.

[24] C. Grossmann, A. Schaefer, and M. F.-X. Wagner, "A finite element study on localized deformation and functional fatigue in pseudoelastic niti strips," *Materials Science and Engineering: A*, vol. 527, no. 45, pp. 1172 – 1178, 2010.

[25] K. Atli, I. Karaman, R. Noebe, and D. Gaydosh, "The effect of training on two-way shape memory effect of binary niti and niti based ternary high temperature shape memory alloys," *Materials Science and Engineering: A*, vol. 560, no. 0, pp. 653 – 666, 2013.

[26] N. G. Jones and D. Dye, "Martensite evolution in a NiTi shape memory alloy when thermal cycling under an applied load," *Intermetallics*, vol. 19, pp. 1348–1358, Oct. 2011.

[27] R. F. Hamilton, H. Sehitoglu, Y. Chumlyakov, and H. J. Maier, "Stress dependence of the hysteresis in single crystal NiTi alloys," *Acta Materialia*, vol. 52, pp. 3383–3402, June 2004.

[28] A. Ibarra, D. Caillard, J. San Juan, and M. L. Nó, "Martensite nucleation on dislocations in Cu–Al–Ni shape memory alloys," *Applied Physics Letters*, vol. 90, no. 10, p. 101907, 2007.

[29] T. Simon, A. Kröger, C. Somsen, A. Dlouhy, and G. Eggeler, "On the multiplication of dislocations during martensitic transformations in NiTi shape memory alloys," *Acta Materialia*, vol. 58, pp. 1850–1860, Mar. 2010.

[30] A. Taylor and R. W. Floyd, "Precision measurements of lattice parameters of non-cubic crystals," *Acta Crystallographica*, vol. 3, pp. 285–289, July 1950.

[31] M. Mueller and H. W. Knott, "The crystal structures of Ti_2Cu, Ti_2Ni, Ti_4Ni_2O, and Ti_4Cu_2O," *Trans. AIME*, vol. 227, pp. 674–678, Jan. 1963.

[32] T. Tadaki, Y. Nakata, K. Shimizu, and K. Otsuka, "Crystal structure, composition and morphology of a precipitate in an aged Ti-51 at. pct Ni shape memory alloy," *Japan Institute of Metals*, vol. 27, pp. 731–740, Jan. 1986.

[33] J. Khalil-Allafi, A. Dlouhy, and G. Eggeler, "Ni_4Ti_3-precipitation during aging of NiTi shape memory alloys and its influence on martensitic phase transformations," *Acta Materialia*, vol. 50, pp. 4255–4274, Oct. 2002.

[34] K. Otsuka and X. Ren, "Physical metallurgy of Ti–Ni-based shape mem-

ory alloys," *Progress in Materials Science*, vol. 50, pp. 511–678, July 2005.

[35] S. Miyazaki and A. Ishida, "Martensitic transformation and shape memory behavior in sputter-deposited TiNi-base thin films," *Materials Science and Engineering A*, vol. 273-275, pp. 106–133, Dec. 1999.

[36] X. Ren, N. Miura, J. Zhang, K. Otsuka, K. Tanaka, M. Koiwa, T. Suzuki, Y. I. Chumlyakov, and M. Asai, "A comparative study of elastic constants of Ti–Ni-based alloys prior to martensitic transformation," *Materials Science and Engineering A*, vol. 312, pp. 196–206, Aug. 2001.

[37] E. L. Semenova and A. L. Tret'yachenko, "The Solidus Surface in the Ti–Ni–Hf System in the Ti TiNi HfNi Hf Region," *Powder Metallurgy and Metal Ceramics*, vol. 40, no. 7-8, pp. 414–425, 2001.

[38] J. E. Daniels and M. Drakopoulos, "High-energy X-ray diffraction using the Pixium 4700 flat-panel detector," *Journal of Synchrotron Radiation*, vol. 16, pp. 463–468, May 2009.

[39] A. P. Hammersley, S. O. Svensson, M. Hanfland, A. N. Fitch, and D. Hausermann, "Two-dimensional detector software: From real detector to idealised image or two-theta scan," *High Pressure Research*, vol. 14, pp. 235–248, Jan. 1996.

[40] H. M. Rietveld, "A profile refinement method for nuclear and magnetic structures," *J Appl Crystallography*, vol. 2, pp. 65–71, June 1969.

[41] A. C. Larson and R. B. Von Dreele, "GSAS: general structure analysis system," *Report lAUR 86-748*, 1994.

[42] B. H. Toby, "EXPGUI, a graphical user interface for GSAS," *Journal Of Applied Crystallography*, vol. 34, pp. 210–213, 2001.

[43] F. Cuevas, M. Latroche, F. Bouree-Vigneron, and A. Percheron-Guegan, "A conjoint XRD-ND analysis of the crystal structures of austenitic and martensitic $Ti_{0.64}Zr_{0.36}Ni$ hydrides," *Journal of Solid State Chemistry*, vol. 179, no. 11, pp. 3295–3307, 2006.

[44] E. H. Majzoub, R. G. Hennig, and K. F. Kelton, "Rietveld refinement and ab initio calculations of a C14-like Laves phase in Ti-Zr-Ni," *Philosophical Magazine Letters*, vol. 83, no. 1, pp. 65–71, 2003.

[45] K. Otsuka, T. Sawamura, and K. Shimizu, "Crystal structure and internal defects of equiatomic TiNi martensite," *Physica Status Solidi (a)*, vol. 5, no. 2, pp. 457–470, 1971.

[46] G. M. Michal and R. Sinclair, "The structure of TiNi martensite," *Acta Crystallographica Section B Structural Crystallography and Crystal Chemistry*, vol. 37, pp. 1803–1807, Oct. 1981.

[47] X. Y. Huang, G. J. Ackland, and K. M. Rabe, "Crystal structures and shape-memory behaviour of NiTi," *Nature Materials*, vol. 2, no. 5, pp. 307–311, 2003.

[48] T. Hahn, ed., *International tables for crystallography: Space-group symmetry*, vol. A. Published by Springer for The international union of crystallography, 5 ed., 2005.

[49] J. C. Slater, "Atomic Radii in Crystals," *The Journal of Chemical Physics*, vol. 41, no. 10, pp. 3199–3204, 1964.

[50] L. Pauling, "Atomic radii and interatomic distances in metals," *Journal of the American Chemical Society*, vol. 69, pp. 542–553, Mar. 1947.

[51] S. Qiu, V. B. Krishnan, S. A. Padula, R. D. Noebe, D. W. Brown, B. Clausen, and R. Vaidyanathan, "Measurement of the lattice plane strain and phase fraction evolution during heating and cooling in shape memory NiTi," *Applied Physics Letters*, vol. 95, no. 14, p. 141906, 2009.

[52] M. A. Azeem, *Diffraction investigations of high temperature shape memory alloys*. PhD thesis, Imperial College London, United Kingdom, 2013.

[53] X. L. Meng, W. Cai, Y. D. Fu, J. X. Zhang, and L. C. Zhao, "Martensite structure in Ti-Ni-Hf-Cu quaternary alloy ribbons containing $(Ti,Hf)_2Ni$ precipitates," *Acta Materialia*, vol. 58, no. 10, pp. 3751–3763, 2010.

[54] M. F. X. Wagner and W. Windl, "Lattice stability, elastic constants and macroscopic moduli of NiTi martensites from first principles," *Acta Materialia*, vol. 56, no. 20, pp. 6232–6245, 2008.

Appendix A: Per cycle evolution of B19′ and B2 lattice

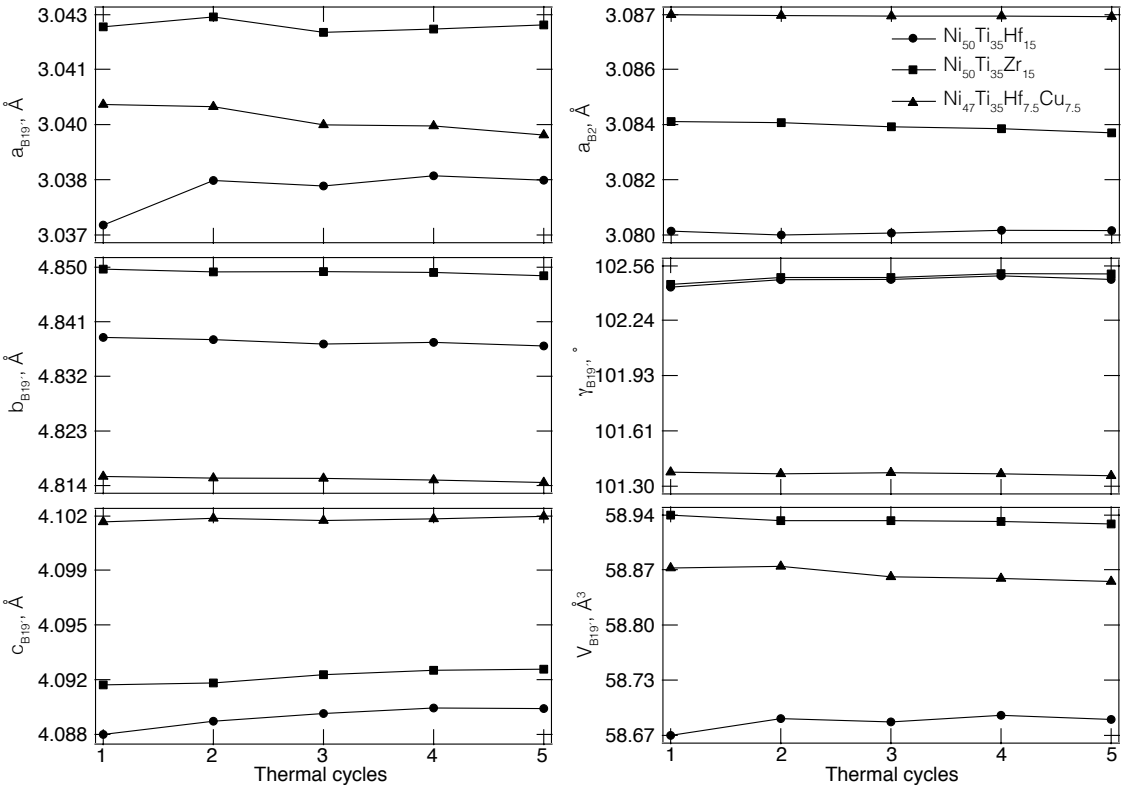

Figure 9: The per cycle evolution of lattice parameters in B2 (at 85 °C) and B19′ (at 265 °C) in $Ni_{50}Ti_{35}Hf_{15}$, $Ni_{50}Ti_{35}Zr_{15}$ and $Ni_{47}Ti_{35}Hf_{7.5}Zr_{7.5}$. Individual values and the corresponding uncertainties are provided in Table 6 below.

Table 6: The per cycle evolution of Rietveld refine B2 and B19′ lattice parameters in $Ni_{50}Ti_{35}Hf_{15}$, $Ni_{50}Ti_{35}Zr_{15}$ and $Ni_{47}Ti_{35}Hf_{7.5}Zr_{7.5}$. Unit cell lengths, monoclinic angle and volume are represented in Å, ° and $Å^3$ respectively and corresponding uncertainties are provided in parenthesis.

Cycle	$a_{B19'}$	$b_{B19'}$	$c_{B19'}$	$\gamma_{B19'}$	$V_{B19'}$	a_{B2}	V_{B2}
			$Ni_{50}Ti_{35}Hf_{15}$				
1	3.0371(3)	4.8384(4)	4.0883(3)	102.43(1)	58.666(7)	3.08030(4)	29.227(1)
2	3.0382(4)	4.8380(5)	4.0891(4)	102.47(1)	58.687(8)	3.08017(4)	29.218(1)
3	3.0381(3)	4.8373(5)	4.0896(3)	102.47(1)	58.683(8)	3.08024(5)	29.225(1)
4	3.0383(4)	4.8376(5)	4.0899(3)	102.49(1)	58.691(9)	3.08033(5)	29.227(1)
5	3.0382(4)	4.8370(5)	4.0899(3)	102.47(1)	58.686(9)	3.08032(5)	29.227(1)
			$Ni_{50}Ti_{35}Zr_{15}$				
1	3.0422(4)	4.8494(6)	4.0914(3)	102.45(3)	58.941(9)	3.08383(8)	29.327(2)
2	3.0424(4)	4.8490(7)	4.0915(3)	102.48(5)	58.93(1)	3.08380(8)	29.326(2)
3	3.0420(4)	4.8490(7)	4.0921(3)	102.49(6)	58.93(1)	3.08366(9)	29.322(3)
4	3.0421(5)	4.8489(7)	4.0923(3)	102.51(6)	58.93(1)	3.08360(9)	29.321(2)
5	3.0422(5)	4.8483(7)	4.0924(3)	102.50(6)	58.93(1)	3.08347(9)	29.317(3)
			$Ni_{47}Ti_{35}Hf_{7.5}Zr_{7.5}$				
1	3.0402(5)	4.8160(7)	4.1018(3)	101.38(2)	58.88(1)	3.08728(6)	29.426(2)
2	3.0401(5)	4.8157(8)	4.1020(3)	101.37(2)	58.88(1)	3.08726(7)	29.425(2)
3	3.0396(5)	4.8156(8)	4.1019(3)	101.38(2)	58.86(1)	3.08724(6)	29.425(2)
4	3.0396(5)	4.8154(8)	4.1020(3)	101.37(2)	58.86(1)	3.08723(6)	29.424(2)
5	3.0394(5)	4.8150(8)	4.1022(3)	101.36(2)	58.86(1)	3.08722(7)	29.424(2)